<div align="center">Supplementary Information</div>

Heterostructured Grafting of NiFe-Layered Double Hydroxide@TiO₂ for Boosting Photoelectrochemical Cathodic Protection

Zhi-Jun Wang[a], Hui Xie[a], Seong Chan Jun[b], Jiang Li[c], Li Cheng Wei[a], Yu Chen Fang[a], Shude Liu[d]*, Ming Ma[c]*, Zheng Xing[a]*

a. School of Chemical Engineering and Technology, Sun Yat-sen University, Zhuhai, 519082, Guangdong, PR China.

b. School of Mechanical Engineering, Yonsei University, Seoul 120-749, South Korea.

c. Shenzhen Institute of Advanced Technology, Chinese Academy of Sciences, Shenzhen 518055, China.

d. College of Textiles, Donghua University, Shanghai 201620, PR. China.

*Corresponding Author.

Email addresses: sdliu@dhu.edu.cn (S. Liu), ming.ma@siat.ac.cn (M. Ma), xingzh7@mail.sysu.edu.cn (Z. Xing)

Experimental

Materials

All chemicals used were of analytical grade and were used as received without any further purification. Titanium butoxide ($C_{16}H_{36}O_4Ti$, purity ≥99.0%,), nickel (II) nitrate hexahydrate ($Ni(NO_3)_2 \cdot 6H_2O$, ≥98%), and iron (III) nitrate nonahydrate ($Fe(NO_3)_3 \cdot 6H_2O$, ≥99.0%) were purchased from Sigma-Aldrich. Ethanol anhydrous (C_2H_6O, ≥99.7%) and acetone (C_3H_6O, ≥98%) were purchased from the General Reagent. Hydrochloric acid (HCl, ≥99.7%, 36.0%-38.0% by weight) was purchased from Sinopharm Chemical Reagent Co., Ltd. Sodium hydroxide (NaOH, ≥95%) was purchased from Macklin. Formamide (CH_3NO, ≥98.0%) was purchased from Sigma-Aldrich

Co. Fluorine-doped tin oxide (FTO, transparency > 84%, sheet resistance: ca. 8 Ω) was purchased from Pilkington OPV-TECH. Deionized and decarbonated water was used in all the experiments.

Fabrication of the photoanode and 304 SS electrode

Preparation of annealed-TiO_2 nanorod arrays (ATNAs): Pristine TNAs photoanodes were fabricated by a modified hydrothermal method.[22] Initially, 64 mL of hydrochloric acid (x = 4, 4.5, 5, 5.5, and 6), and 0.8 mL of titanium butoxide were mixed in a Teflon-lined autoclave (100 mL). 6-7 pieces of FTO glass (10×20 mm^2) were then placed on a Teflon liner at 60° to the bottom. Subsequently, the autoclave was heated at 150 °C for 20 h and cooled via y ways (y = furnace cooling and water cooling). After rinsing with deionized water and drying with N_2 gas, TNAs were obtained. In addition, the as-prepared TNAs were annealed at 500 °C for 2 h at a rate of z °C/min (z = 1, 5, 10, 15, and 20) to obtain the ATNAs.

Preparation of a colloidal suspension of ultrathin Ni-Fe LDH nanosheets (NiFe-LDH NSs).[23] 2.1810 g $Ni(NO_3)_2 \cdot 6H_2O$ and 1.009 g $Fe(NO_3)_3 \cdot 9H_2O$ were added to 200 mL of deionized water and mixed with 200 mL of a 23 vol% formamide (layer growth inhibitor) solution under magnetic stirring, at 80 °C. Simultaneously, 0.25 M NaOH was slowly added dropwise into the solution to maintain a pH of approximately 10 and inhibit cationic hydrolysis. The reaction was complete within 10 min. After cooling to room temperature, the precursor was collected by centrifugation at 5000 rpm for 5 min and washed with a mixture of ethanol and DI water (1:1 vol) several times. The centrifugal substrates were kept in a wet state and divided into different masses for subsequent use. The wet substrates of different masses (0.08–0.64 g) were dispersed in 20 mL of formamide and then subjected to 8 h of ultrasonic exfoliation. The conditions of the ultrasonication treatment involved on/off pulses every 1.5 s with a power of 650 W (9%), while the surroundings were maintained at freezing temperatures using an ultrasonic crusher (SCIENTZ, JY 92-IIN, 650 W). Different concentrations of colloidal suspensions of the NiFe-LDH NSs were centrifuged at 2000 rpm for 10 min to remove any residual large Ni-Fe LDH NSs, and ultrathin NiFe-LDH NSs were collected by high-speed centrifugation (12000 rpm for 1.5 h) for material

characterization.

Preparation of NiFe-LDH NSs/ATNAs (NF-ATNAs): The as-prepared ATNAs were immersed in x g/L (x = 4, 8, 12, 16, 20, 24, 28, and 32) colloidal suspensions of the NiFe-LDH NSs for y h (y = 1, 1.5, 2, 2.5, 3, 3.5, and 4), to deposit the NiFe-LDH NSs on the interarrays and surface of the ATNAs. When the deposition was completed, the surface liquid of NF-ATNAs was blown dry with N_2 gas, and then they were placed in a vacuum drying oven at 40 °C for ca. 30 min.

Preparation of 304 SS electrode: The back side of a commercial 304 SS sheet was welded to a copper wire. Subsequently, it was encapsulated with epoxy resin, and the front side of the 304 SS was exposed.

Materials characterization

The morphology, microstructure, and elemental distribution were analyzed using scanning electron microscope, transmission electron microscopy images, and element distribution maps from a field-emission Gemini SEM 500 and Hitachi TEM HT7800. X-ray diffraction patterns were examined by Rigaku XRD Ultima IV (with cu Kα-radiation and I=1.5406 Å). The ultraviolet-visible diffuse reflectance spectra of the photoanodes in solid phases were recorded using a UV-vis-NIR spectrophotometer (Shimadzu UV 3600) equipped with an integrating sphere (non-use of the NiFe-LDH NSs sample) with $BaSO_4$ as a reference. The Thermo-VG Scientific Nexsa G2 XPS (with monochromatic Al Kα X-ray source) was used to obtain the X-ray photoelectron spectroscopy survey and high-resolution spectra of the samples. All binding energy values were referenced to the C1s peak of hydrocarbons at 284.8 eV. Raman spectra of the samples were obtained using a Renishaw inVia Raman microscope (532 nm Raman laser, power 10%).

Photoelectrochemical measurements

Photoelectrochemical performances of photoanodes were evaluated in a typical three-electrode configuration (RE: Ag/AgCl electrode (4M KCl), CE: 10 × 10 mm^2 platinum sheet), and the PECCP system was evaluated using the equipment shown in Fig. S2, which utilized a CHI 660E electrochemical workstation for PEC

performance testing. A solar simulator (AM 1.5 G, Peccell Technologies, Inc., Yokohama, Japan) and a 300 W xenon lamp (PLS-SXE300+, AM 1.5 G, tested by a PerfectLight detector) were used as the light source, and the illumination area were set as 15 cm^2 and 7.1 cm^2. The electrochemical environment of the PECCP system was tested in 0.5 M sodium sulfate (Na$_2$SO$_4$, pH 6.6) and 3.5 wt.% sodium chloride (NaCl, pH 6.8) for the photoanode and 304 SS, respectively. The photocurrent densities under chopped illumination were monitored by sweeping the positive direction at a scan rate of 20 mV/s for J-V diagrams or by applying a constant bias for J-t diagrams; the areas of all photoanodes dipped in the electrolyte were 10 × 10 mm^2. All results in this paper are presented against reversible hydrogen electrodes (RHEs), and the conversion between potentials vs. Ag/AgCl and vs. RHE was performed using the following equation:

$$E \text{ (vs. RHE)} = E \text{ (vs. Ag/AgCl)} + E_{4 \text{ M Ag/AgCl}} \text{ (reference)} + 0.0591 \times \text{pH}$$

$$(E_{4 \text{ M Ag/AgCl}} \text{ (reference)} = 0.1976 \text{ V vs. NHE at 298 K})$$

Electrochemical impedance spectroscopy (AC voltage: 10 mV and frequency range of 10^5–10^{-2} Hz) and Mott-Schottky (potential range: -1–1 V vs. Ag/AgCl and test frequency: 3 kHz) measurements were performed using a Gamry 3000 electrochemical station.
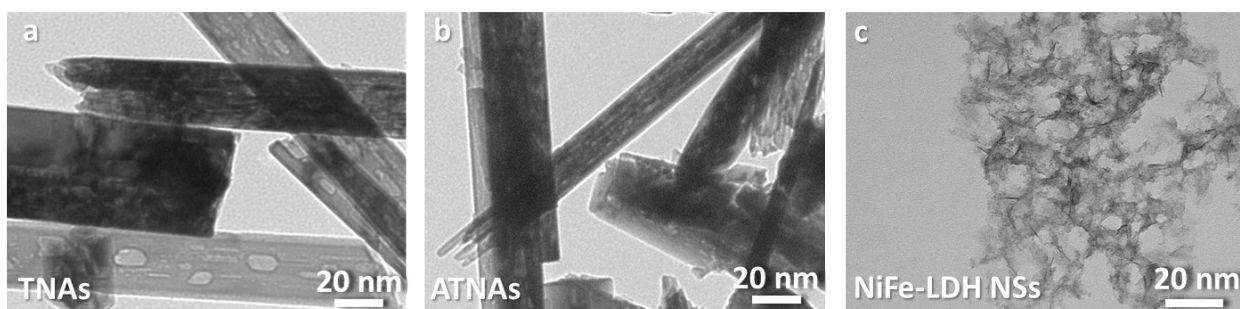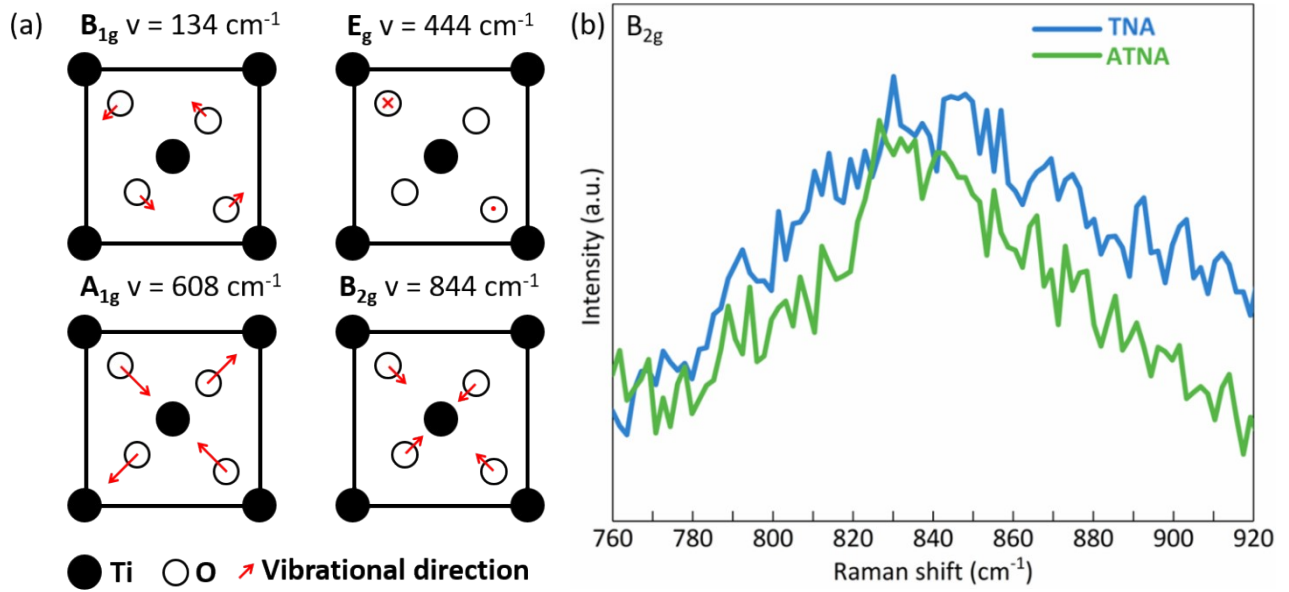
Supplementary Figures
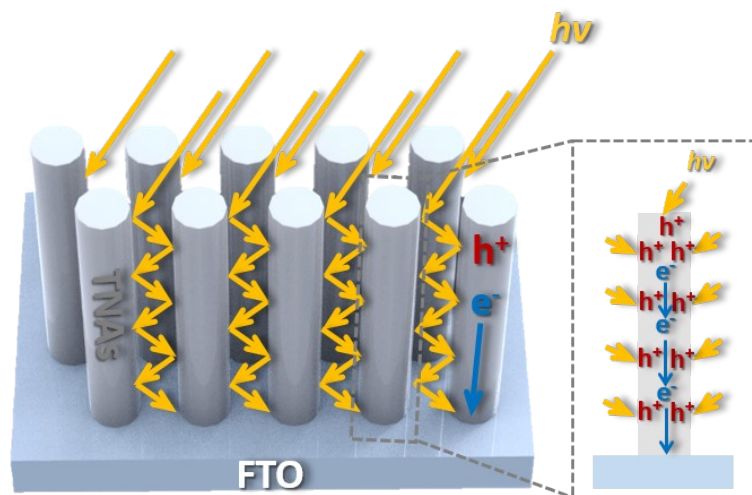
Supplementary Fig. 1: Scheme of the light trapping process in TNAs. The ideal pathway of photoexcited

electrons will smooth transfer to FTO by the 1D vertical structure.
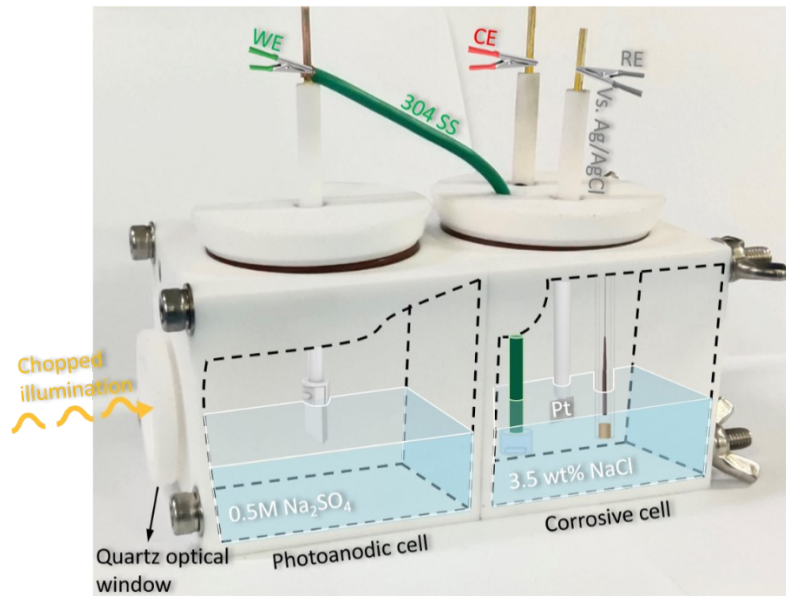
Supplementary Fig. 2: The equipment for evaluating the PECCP system.

Supplementary Fig. 3: The TEM images of components. TEM images of (a) TNAs, (b) ATNAs, and (c) NiFe-LDH NSs.

Supplementary Fig. 4: Atomic vibrations and Raman spectra of rutile-TiO$_2$. (a) Scheme of Raman active atomic vibrations in rutile-TiO$_2$. (red arrows represent the amplitudes of vibrations). In Raman spectra, the E$_g$ mode was dominantly caused by the symmetric stretching vibration of O-Ti-O, and the B$_{1g}$ mode was caused by symmetric bending vibration (the A$_{1g}$ mode was caused by anti-symmetric bending vibration).[3] **(b)** Raman spectra of B$_{2g}$ mode in TNAs and ATNAs.
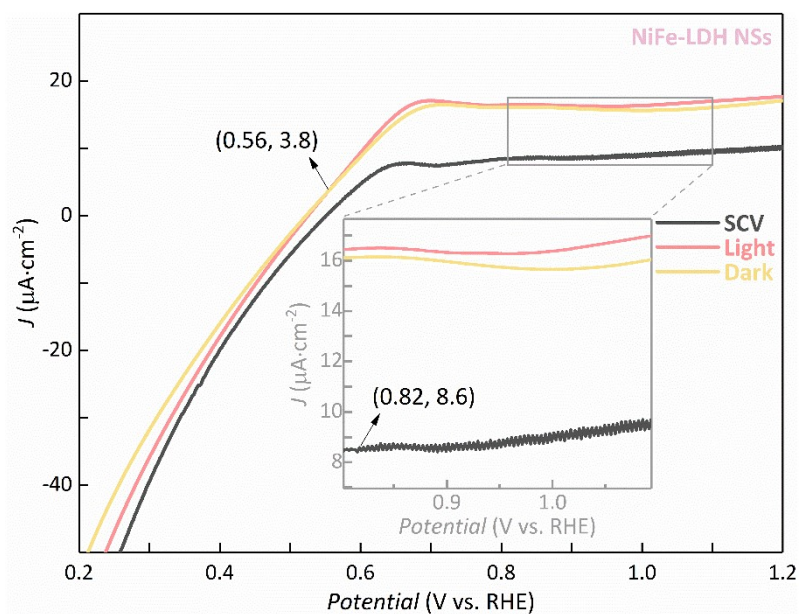
Supplementary Fig. 5: Photograph records of the NiFe-LDH NSs dispersed in formamide. (a) The 4–32 g/L concentrations of NiFe-LDH NSs and (**b**) the Tyndall effect of 28 g/L NiFe-LDH NSs colloidal suspension.
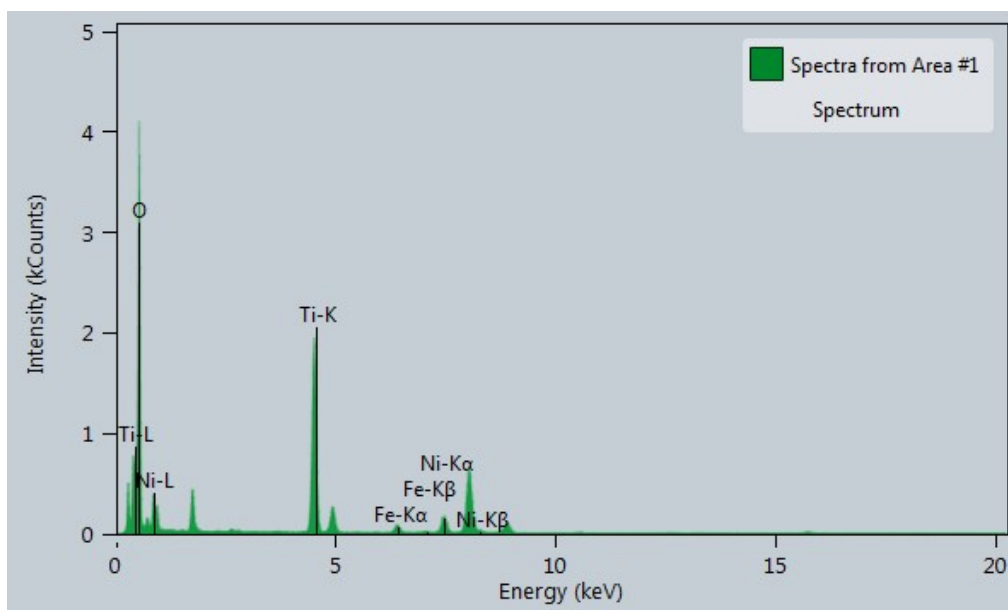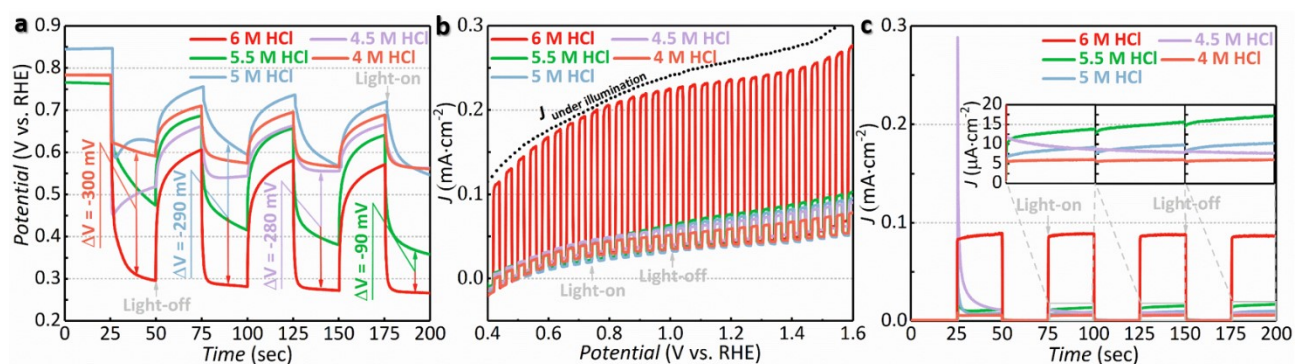
Supplementary Fig. 6: The detailed EDS mapping information of NF-ATNAs.

Supplementary Fig. 7: SCV and LSV scans of the NiFe-LDH NSs.

The NiFe-LDH NSs electrode was fabricated via a drop-casting method. Taken 120 μL 28 g/L NiFe-LDH NSs suspension and dropped onto FTO surface with 80 °C hot-plat, then blown dry with N_2 gas and placed in a vacuum drying oven at 40 °C for ca. 30 minutes.
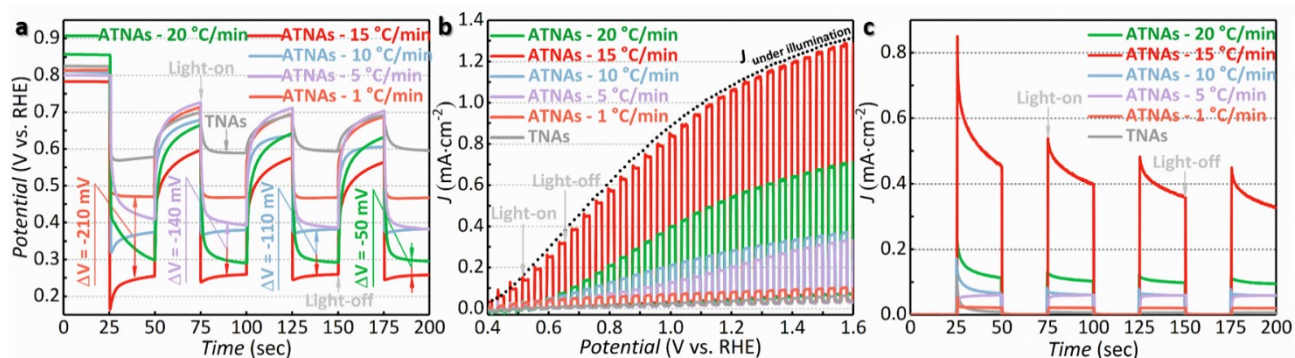
Supplementary Fig. 8: PEC Performance of changed HCl concentrations in range 4 to 6 M for preparing pristine TNAs. (a) OCV curves, (**b**) LSV curves (shutter with 1 s interval, 10 mV/s scan rate), and (**c**) Current densities-time (J-t, partial voltage was ca. 0.8 V vs. RHE, according to OCV of photoelectrode in dark) curves of various HCl concentrations (4–6 M) of TNAs upon 25 s/25 s interval irradiation.

As shown in Fig. S7, the OCP maximum value was -500 mV (6 M HCl) with the minimum E_{ps} potential of 0.28 V vs. RHE, and the as-prepared pristine TNAs -6 M HCl also clearly obtained a high transient photocurrent density (TPCD).
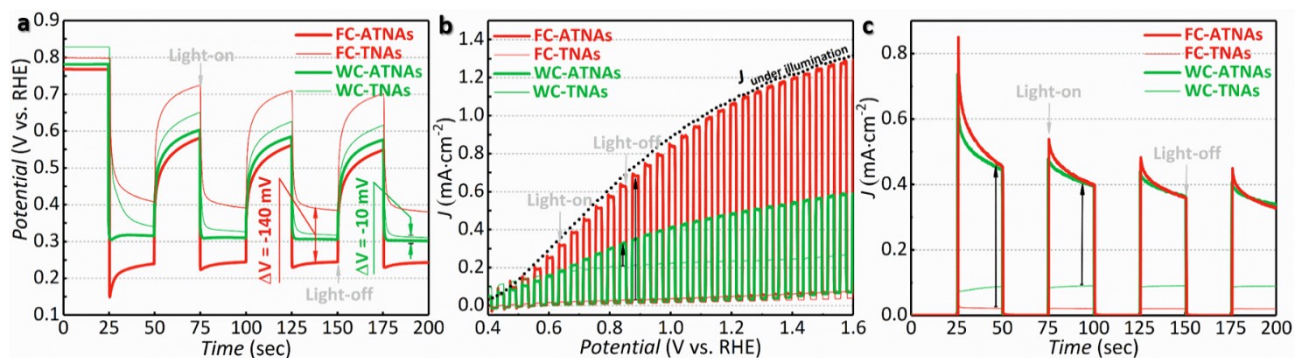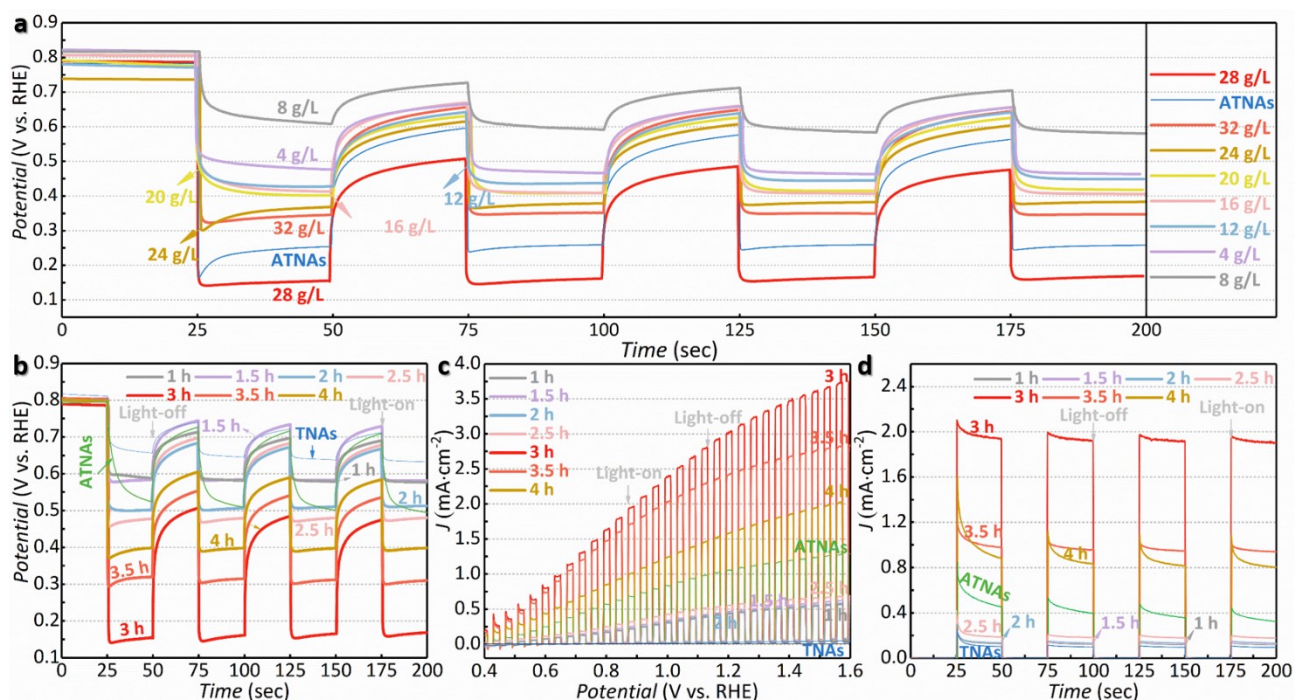
Supplementary Fig. 9: PEC performance of different cooling ways and after annealing of the pristine TNAs and ATNAs. (a) OCV curves, **(b)** LSV curves (shutter with 1 s interval) and **(c)** J-t curves of both cooling ways (furnace cooling, FC; Water cooling, WC) of pristine TNAs and ATNAs upon 25 s/25 s interval irradiation.

As shown in Fig. S8, the OCP maximum value was -450 mV (WC-pristine TNA) with the minimum E_{ps} potential of 0.35 V vs. RHE, however, after annealing ramp of 15 °C/min, the as-prepared FC-ATNAs (be used in manuscript) obtained stronger PEC performance (OCP maximum value was -550 mV with the minimum E_{ps} potential of 0.25 V vs. RHE). It was probably due to the larger crystal sizes, which were vulnerable to being broken because of the inter-force of nanorods after annealing, obtained via the WC method influenced the PEC performance of WC-ATNAs.

Supplementary Fig. 10: PEC performance of changed annealing ramps in range 1 to 20 ºC/min for preparing ATNAs. (**a**) OCV curves, (**b**) LSV curves (shutter with 1 s interval), and (**c**) J-t curves of various ramp rates (1–20 °C/min) of the ATNAs upon 25 s/25 s interval irradiation.

As shown in Fig. S9, the OCP maximum value was -550 mV (ATNA-15 °C/min) with the minimum E_{ps} potential of 0.25 V vs. RHE and the as-prepared ATNAs-15 °C/min also clearly obtained a high TPCD.

Supplementary Fig. 11: PEC performance of different concentrations and self-assembly time of the NiFe-LDH NSs for preparing NF-ATNAs. (**a**) OCV curves of different concentrations with 3 h self-assembly time (4–32 g/L) upon 25 s/25 s interval irradiation. (**b**) OCV curves, (**c**) LSV curves (shutter with 1 s interval) and (**d**) J-t curves of different self-assemble time (1–4 h) of 28 g/L NiFe-LDH NSs upon 25 s/25 s interval irradiation.

As shown in Fig. S11a&b, the OCPV maximum value was -650 mV (NF-ATNAs-28 g/L NiFe-LDH NSs&3 h self-assemble time, which were used in manuscript) with the minimum E_{ps} potential of 0.15 V vs. RHE.

Despite pristine TNAs (such as TNAs-4.5 M HCl) and ATNA (such as FC-ATNAs-15 °C/min) possessed TPCDs of 0.01 and 0.5 mA/cm², the trouble of severe surface carriers recombination, which exhibited current spikes at transient "light-on", will weaken the PEC performance of photoanodes (shown in J-t curves). Herein, it is to be noted that the introduction of the NiFe-LDH NSs on ATNAs alleviated this crippling effect and possessed a higher TPCD of 2.0 mA/cm².[4–7]
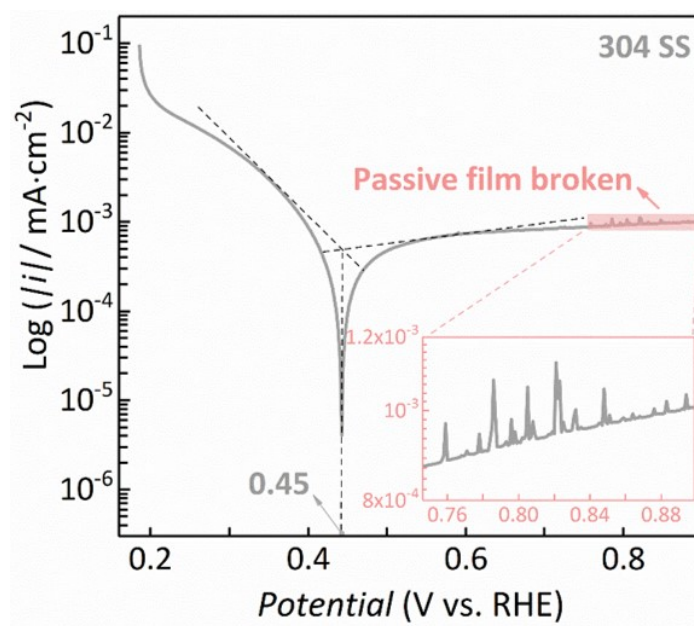
Supplementary Fig. 12: The Tafel plot (scan rate = 0.1667 mV/s) of bare 304 SS in the corrosive cell. The

inset image was the broken current of the passive film.
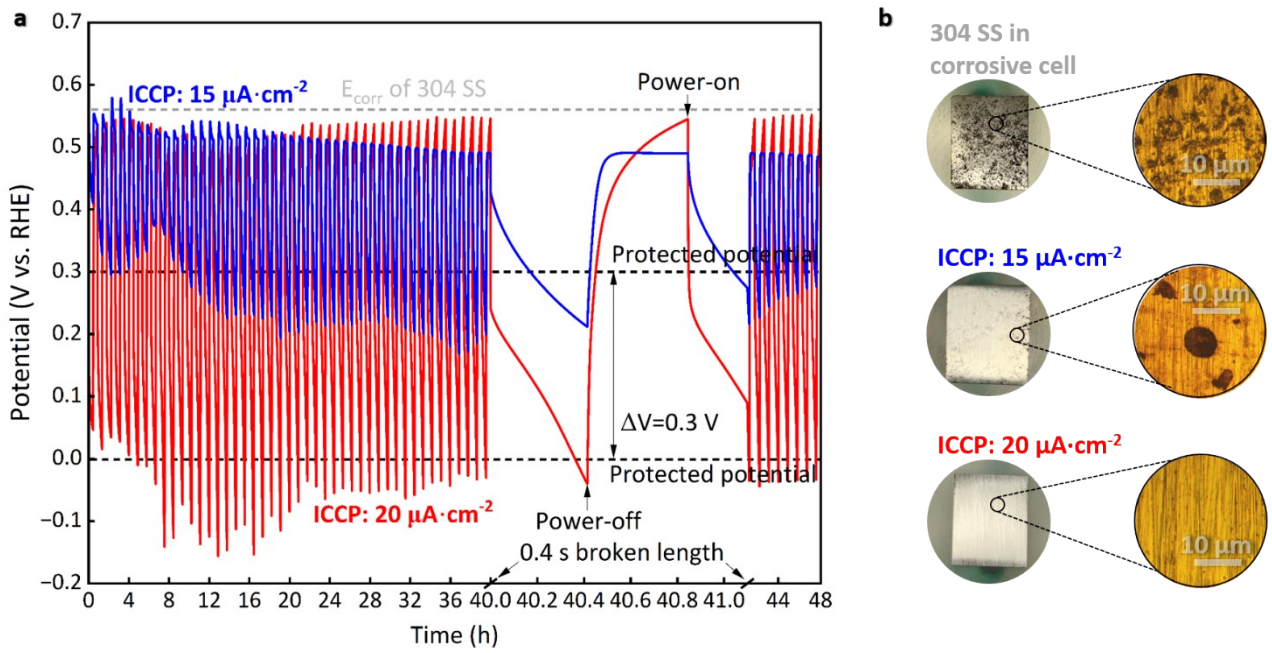
Supplementary Fig. 13: The impressed current cathodic protection (ICCP) of 304 SS in the corrosive cell.

(**a**) OCV curves of different impressed current densities (15 and 20 μA$\cdot$cm^{-2}), accordingly, (**b**) optical images of bare 304 SS and coupled with different impressed current densities in the corrosive cell.
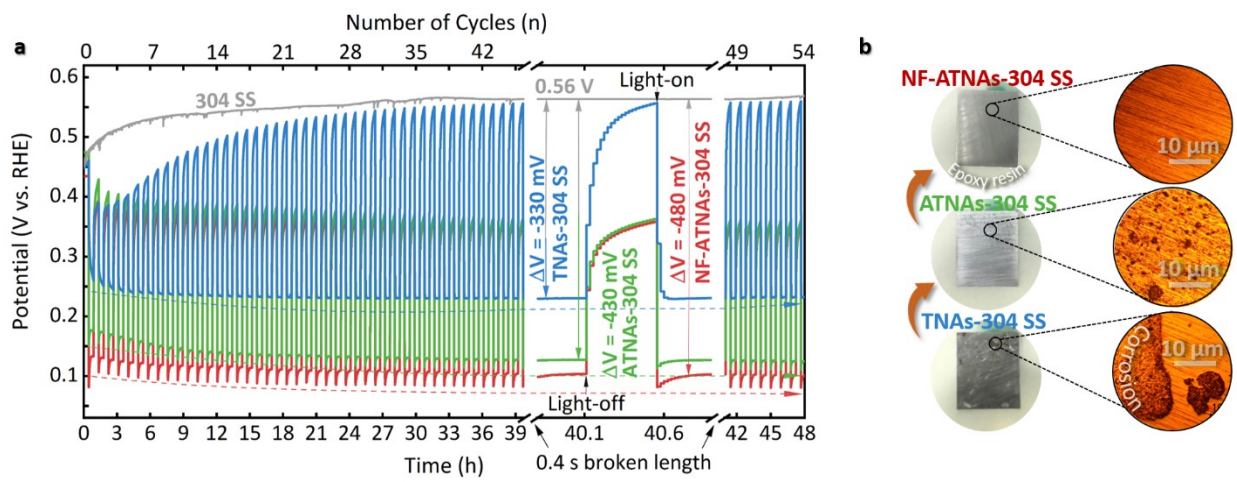
Supplementary Fig. 14: The results of all the 304 SS couples under xenon lamp irradiation in the corrosive cell. (**a**) OCV curves, (**b**) optical images of 304 SS coupled with TNAs, ATNAs, and NF-ATNAs, respectively.
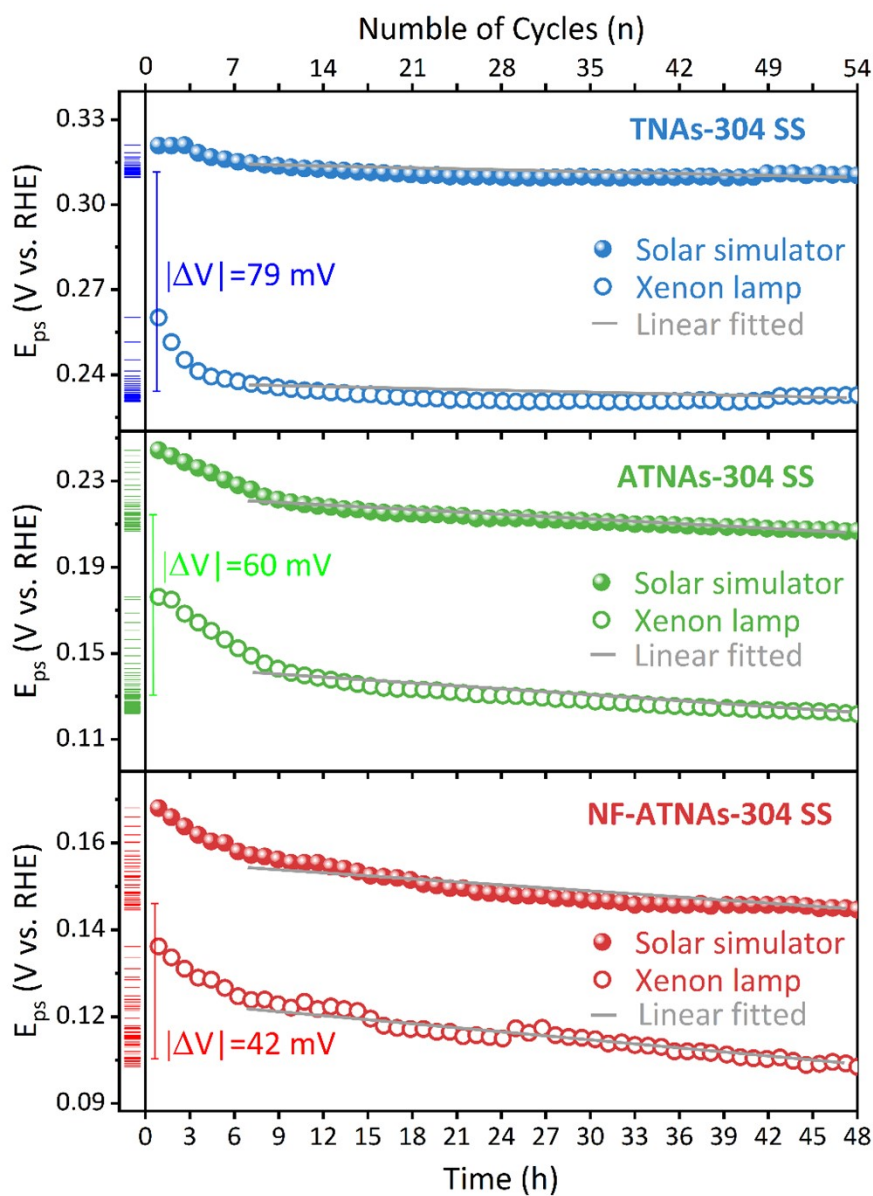
Supplementary Fig. 15: The change of E_{ps} upon cyclic illumination observed with TNAs-304 SS, ATNAs-304 SS, and NF-ATNAs-304 SS under different lighting condition.
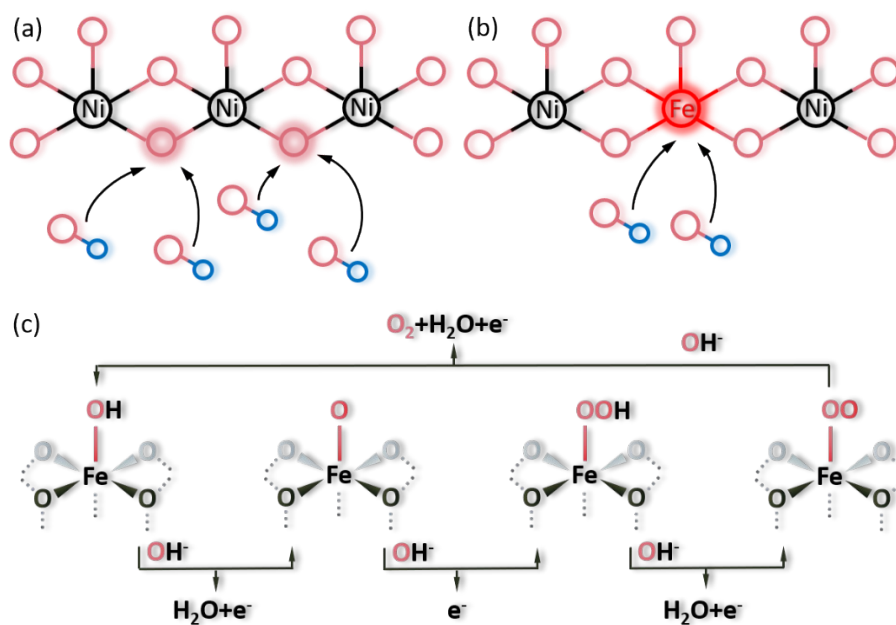
Supplementary Fig. 16: Scheme of surface Fe atomic catalyst in OER process. (**a**) Participation of NiOOH lattice oxygen in OER process. (**b**) Fe atom instead of Ni atom in OER process. (**c**) Special OER process of Fe atom in NiFe LDHs.

The Fe atoms in NiFe LDHs / Fe-doped γ-NiOOH, which was oxidized from Fe-doped α-Ni(OH)$_2$ via a thermal treatment, were the true active site and serviced as "no-mass-consumption" catalysts in OER process.[8,9]

Supplementary Tables

Supplementary Table 1. The elemental atomic content (%) of all samples.

	Fe	Ni	Ti	O	C
NF-ATNAs	2.01	6.22	17.67	42.04	32.06
NiFe-LDH NSs	6.50 (2p)	18.29 (2p)	-	53.45	21.76
	6.93 (3s)	18.58 (3s)	-	54.36	20.13
ATNAs	-	-	12.53	48.66	38.81
pristine TNAs	-	-	12.49	57.92	29.59

Notes: for further quantification of the atomic content of Ni and Fe elements, the Ni 3s and Fe 3s were used to compare those of Ni 2p and Fe 2p orbitals in the NiFe-LDH NSs.

Supplementary Table 2. The previous efforts summary on PEC performance of TiO$_2$.

Year	Method	OCP (Δ V)	Photoanodic electrolyte	Reference
2010	AO	-380 mV	0.2 M NaOH + 0.1 M Na$_2$S	[10]
2014	AO	-120 mV	-	[11]
2015	AO	-200 mV	-	[12]
2016	AO	-50 mV	0.2 M NaOH + 0.1 M Na$_2$S	[13]
2017	HT	-100 mV	0.2 M NaOH + 0.1 M Na$_2$S	[14]
2020	AO	-100 mV	0.2 M NaOH + 0.1 M Na$_2$S	[15]
2021	AO	-180 mV	0.25 M Na2S + 0.35 M Na$_2$SO$_3$	[16]
2022	HT	-75 mV	0.2 M NaOH + 0.1 M Na$_2$S	[17]
	HT	**-500 mV**	**0.5 M Na$_2$SO$_4$**	**This work**

Notes: anodic oxidation (AO); hydrothermal method (HT); open circuit photovoltage (OCP).

Supplementary Table 3. Comparison of SCV and LSV scans with on-set potentials & photocurrent densities at on-set potential.

-	On-set potentials (V vs. RHE)	Photocurrent densities at on-set potential ($\mu A \cdot cm^{-2}$)
pristine TNAs (LSV)	0.329	-
pristine TNAs (SCV)	0.167	0.28
ATNAs (LSV)	0.118	-
ATNAs (SCV)	0.133	0.81
NF-ATNAs (LSV)	0.100	-
NF-ATNAs (SCV)	0.085	3.69

Reference

[1] S. W. Kwon, M. Ma, M. J. Jeong, K. Zhang, S. J. Kim and J. H. Park, *ChemComm*, 2016, **52**, 13807.

[2] Y. F. Zhao, X. Zhang, X. D. Jia, G. I. N. Waterhouse, R. Shi, X. R. Zhang, F. Zhan, Y. Tao, L. Z. WU, C. H. Tung, D. O'Hare and T. R. Zhang, *Adv. Energy Mater.*, 2018, **8**, 1703585.

[3] O. Frank, M. Zukalova, B. Laskova, J. Kürti, J. Koltai and A. Kavan, *Phys. Chem. Chem. Phys.*, 2012, **14**, 14567.

[4] Y. M. Ma, S. R. Pendlebury, A. Reynal, F. L. Formal and J. R. Durrant, *Chem. Sci.*, 2014, **5**, 2964.

[5] F. F. Abdi and R. Van De Krol, *J. Phys. Chem. C*, 2012, **116**, 9398.

[6] F. F. Le, K. Sivula and M. Grätzel, J. Phys. Chem. C, 2012, **116**, 26707.

[7] L. M. Peter, *J. Solid. State. Electrochem.*, 2013, **17**, 315.

[8] J. W. Zhao, Z. X. Shi,C. F. Li, C. Zhao, H. R. Zhang, M. Z. Zhu, Q. Xu, X. Q. Wang, C. M. Zhao, Y. T. Qu, Z. K. Yang, T. Yao, Y. F. Li, Y. Lin, Y. Wu and Y. D. Li, *Chem. Sci.*, 2021, **12**, 650.

[9] H. Shin, H. Xiao and W. A. Goddard III, *J. Am. Chem. Soc.*, 2018, **140**, 6745.

[10] Z. Q. Lin, Y. K. Lai, R. G. Hu, J. Li, R. G. Du and C. J. Lin, *Electrochim. Acta*, 2010, **55**, 8717.

[11] H. Li, X. Wang, Y. Liu and B. R. Hou, *Corros. Sci.*, 2014, **82**, 145.

[12] J. Zhang, Hu J, Y. F. Zhu, Q. Liu, H. Zhang, R. G. Du and C. J. Lin, *Corros. Sci.*, 2015, **99**, 118.

[13] J. Ren, B. Qian, J. Li, Z. W. Song, L. Hao and J. S. Shi, *Corros. Sci.*, 2016, **111**, 596.

[14] J. Hu, Z. C. Guan, Y. Liang, J. Z. Zhou, Q. Lin, H. P. Wang, H. Zhang, and R. G. Du, *Corros. Sci.*, 2017, **125**, 59.

[15] J. T. Zhang, H. L. Yang, Y. Wang, X. H. Cui, Z. Wen, Y. P. Liu, L. Fan and J. T. Feng, *Corros. Sci.*, 2020, **176**, 108927.

[16] X. M. Ma, Z. Ma, D. Z. Lu, Q. T. Jiang, L. L. Li, T. Liao and B. H. Hou, *J. Mater. Sci. Technol.*, 2021, **64**, 21.

[17] Y. P. Liu, J. M. Lu, W. L. Zhang, C. Z. Lin, Z. Y. Wang, X. Wang, H. Xu, J. T. Feng, B. Hou, W. Yan and Z. J. Ren, *Chem. Eng. J.*, 2021, **421**, 127858.